

**HyspIRI Visible to Short Wavelength InfraRed
(VSWIR)
Water Leaving Reflectance
Algorithm Theoretical Basis Document (ATBD)**



Version: August 2010

Bo-Cai Gao

Remote Sensing Division, Code 7230, Naval Research Laboratory
4555 Overlook Avenue, SW, Washington, DC 20375

TABLE OF CONTENTS

SUMMARY	3
1 INTRODUCTION	4
2 OVERVIEW AND BACKGROUND INFORMATION.....	4
2.1 Experimental Objective	4
2.2 Historical Perspective.....	5
2.2.1 The imaging spectrometry concept	5
2.2.2 Radiative transfer modeling approaches for water surfaces	6
2.3 Instrument Characteristics.....	7
3 ALGORITHM DESCRIPTION	10
3.1 Theoretical Description	10
3.1.1 Physics of the problem	10
3.1.2 Mathematical description of the algorithm.....	10
3.1.3 Algorithm implementations	14
3.1.4 Descriptions of input and output data.....	22
3.1.5 Variance and uncertainty estimates	22
3.2 Practical Considerations.....	23
3.2.1 Numerical computation considerations	23
3.2.2 Programming/procedural considerations	23
4 SAMPLE RESULTS.....	23
5. RESEARCH AGEND.....	31
6. REFERENCES.....	31

SUMMARY

This algorithm theoretical basis document (ATBD) describes an algorithm for retrieving the Level 2 water leaving reflectance data products from the Visible ShortWave InfraRed (VSWIR) Level 1b calibrated radiance data. It is in preparation for the possible near future NASA Hyperspectral Infrared Imager (HyspIRI) mission, a Decadal Survey Mission recommended by the National Research Council (NRC). VSWIR, an imaging spectrometer covering the solar spectral region between 0.38 and 2.5 micron with a spatial resolution of 60 m, is one of the two instruments planned for the HyspIRI mission to produce global observations of multiple Earth surface attributes for a variety of terrestrial and aquatic studies.

The radiances received by the VSWIR instrument in the solar spectral region are affected by absorption and scattering effects from atmospheric gases and aerosols. In order to use the VSWIR data for quantitative studies of water properties over deep blue oceans, turbid coastal areas, and inland lakes, the atmospheric effects need to be removed. In this ATBD, we describe a radiative transfer modeling based atmospheric correction approach for the retrieval of water leaving reflectances on a pixel-by-pixel basis from VSWIR data. The descriptions include all elements for corrections, such as atmospheric gases, aerosols, and thin cirrus clouds, journal literature backing up the approach, theoretical descriptions on algorithm's physics and mathematical background, and sample retrieval results, including the removal of sunglint effects, from spectral imaging data collected with the NASA JPL Airborne Visible Infrared Imaging Spectrometer (AVIRIS).

1 INTRODUCTION

This document describes an algorithm for retrieving the Level 2 water leaving reflectance data products from the Visible ShortWave InfraRed (VSWIR) Level 1b calibrated radiance data. It is in preparation for the possible near future NASA Hyperspectral Infrared Imager (HypIRI) mission, a Decadal Survey Mission recommended by the National Research Council (NRC). VSWIR, an imaging spectrometer covering the solar spectral region between 0.38 and 2.5 micron with a spatial resolution of 60 m, is one of the two instruments planned for the HypIRI mission to produce global observations of multiple Earth surface attributes for a variety of terrestrial and aquatic studies.

The radiances received by the VSWIR instrument in the solar spectral region are affected by absorption and scattering effects from atmospheric gases and aerosols. In order to use the VSWIR data for quantitative studies of water properties over clear blue oceans, turbid coastal areas, and inland lakes, the atmospheric effects need to be removed. In this algorithm theoretical basis document (ATBD), we describe a radiative transfer modeling based atmospheric correction approach for the retrieval of water leaving reflectances on a pixel-by-pixel basis from VSWIR data. The descriptions include all elements for corrections, such as atmospheric gases, aerosols, and thin cirrus clouds, journal literature backing up the approach, theoretical descriptions on algorithm's physics and mathematical background, and sample retrieval results, including the removal of sunglint effects, from spectral imaging data collected with the NASA JPL Airborne Visible Infrared Imaging Spectrometer (AVIRIS) (Vane et al., 1993; Green et al., 1998).

Background information on the concept of imaging spectrometry, atmospheric corrections over ocean, and the VSWIR instrument characteristics is described in Section 2. Detailed description of the ocean version of the hyperspectral atmospheric algorithm is presented in Section 3. Sample results from analysis of AVIRIS data are presented in Section 4. Research agenda are described in Section 5.

2 OVERVIEW AND BACKGROUND INFORMATION

The objectives of this algorithm, the historical perspective on atmospheric corrections over water surfaces, and the unique features of the VSWIR instrument, are described in this section.

2.1 Experimental Objective

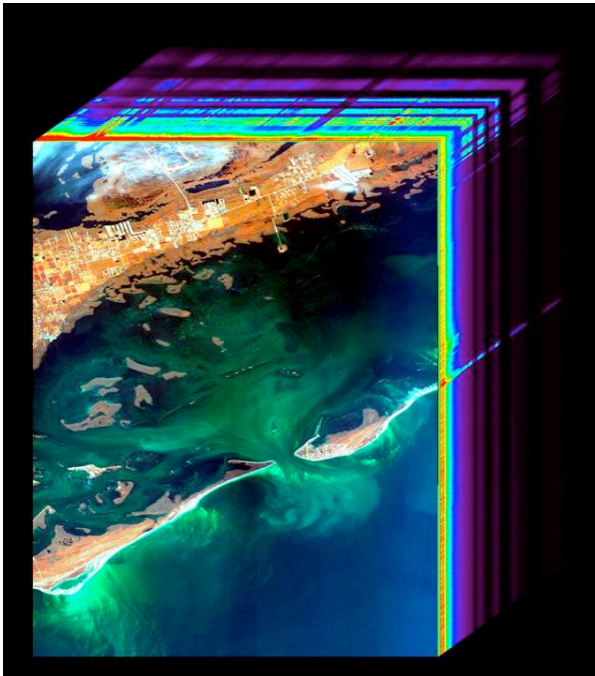
The purpose of this algorithm is to derive water leaving reflectance spectra over the deep blue oceans, turbid coastal areas, and inland lakes of the globe. The data

products will be used for a variety of applications, and to answer many key science questions originally identified in the National Research Council Decadal Survey and recently refined by the HypIRI Science Study Groups and research community. These questions include, but not limited to: What is the composition, function, and health of land and water ecosystems? How are these ecosystems being altered by human activities and natural causes? How do these changes affect fundamental ecosystem processes upon which life on Earth depends?

2.2 Historical Perspective

2.2.1 The imaging spectrometry concept

(A)



(B)

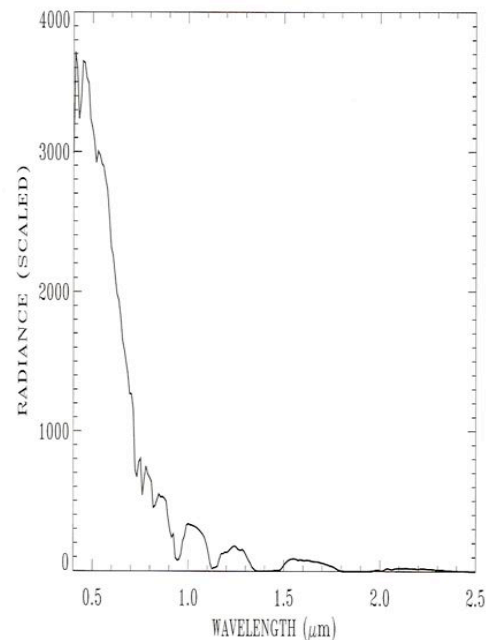


Fig. 1. (a) - an example of 3-dimensional imaging spectrometer data cube downloaded from a web site, and (b) – a sample AVIRIS radiance spectrum over water.

The concept of imaging spectrometry, or hyperspectral imaging of the Earth, originated at the NASA Jet Propulsion Laboratory (JPL) in the early 1980s. Imaging spectrometers acquire images in many contiguous spectral channels such that for each picture element (pixel) a complete reflectance or emittance spectrum can be derived from the wavelength region covered (Goetz et al., 1985). Figure 1a shows an example of 3-dimensional imaging spectrometer data cube (2D spatial and 1D spectral) downloaded from a web site. Figure 1b shows a sample AVIRIS radiance spectrum for a water pixel. The solar radiation on the Sun-surface-sensor ray path is subject to

absorption and scattering by the atmosphere and the surface. Major atmospheric water vapor absorption bands centered at approximately 0.94, 1.14, 1.38 and 1.88 μm , an oxygen absorption band at 0.76 μm , and a carbon dioxide absorption band near 2.08 μm are seen in the spectrum. The shorter wavelength region below 1 μm is also affected by molecular and aerosol scattering.

There is growing interest in hyperspectral remote sensing for research and applications in a variety of fields, including geology, agriculture, forestry, coastal and inland water studies, environment hazards assessment, and urban studies (Davis et al., 2002). In order to study water properties using imaging spectrometer data, very accurate removal of atmospheric absorption and scattering effects is required. This process, called atmospheric correction, is essential to convert radiances measured by the sensors to water leaving reflectances.

2.2.2 Radiative transfer modeling approaches for water surfaces

Over the past three decades, multi-channel atmospheric correction algorithms for applications to case 1 waters (i.e., clear deep ocean waters) have been developed by Howard Gordon's research group at University of Miami. The complexity of the algorithms has been increased greatly with time - from the early single scattering algorithm used for CZCS (Gordon, 1978) to the present more complete multiple scattering algorithm for SeaWiFS (Gordon and Wang, 1994). For the operational SeaWiFS algorithm, a simplified two-layer atmosphere system, i.e., aerosols being confined in the bottom boundary layer and atmospheric gaseous molecules being located in another layer above the aerosol layer, is assumed. An aerosol model and an aerosol optical depth are derived from channels located between 0.76 and 0.87 μm by assuming water leaving radiances to be zero in the spectral range. A sophisticated lookup table procedure is used for the aerosol retrievals. The atmospheric path radiances in the visible are predicted based on the derived aerosol information. The difference between the measured radiances above the atmosphere-ocean system and the predicted path radiance is the water leaving radiance transmitted to the top of the atmosphere.

The SeaWiFS algorithm is quite successful when used for the processing of multi-channel SeaWiFS data, particularly after the radiometric calibration coefficients of SeaWiFS channels are adjusted based on theoretical simulations using the same radiative transfer code as the one used in the generation of lookup tables. The adjustment of calibration coefficients largely removes systematic errors in both the radiative transfer code and the radiometric calibrations. However, minor defects are still present in the SeaWiFS algorithm. For example, the algorithm can produce incorrect water leaving radiances in the visible when applied to pixels in the fringe of

sun glint (Fraser et al., 1997), because the lookup tables used in the algorithm were generated with a radiative transfer code assuming a flat ocean surface, instead of wind-roughened water surface.

Another operational atmospheric correction algorithm for ocean color applications has been under development for many years (Fraser et al., 1997). This algorithm is also implemented for processing CZCS data at a computing facility in NASA Goddard Space Flight Center. The algorithm uses pre-computed lookup tables generated with a vector radiative transfer code (Ahmad and Fraser, 1982) that takes account of the rough ocean surface reflection, a multi-layered atmosphere with mixtures of aerosols and gaseous molecules in each layer, degree of polarization of the light, and multiple scattering. The information about aerosols is derived from the $0.67 \mu\text{m}$ channel. In test retrievals, the derived water leaving radiances in the visible channels agreed to a few percent when both the Fraser algorithm and a version of Gordon's CZCS algorithm were applied to the same CZCS data sets acquired over clear oceanic waters without contamination by sun glint. However, the derived water leaving radiances in the visible differed by approximately 30% when both algorithms were applied to CZCS data with weak contamination by sun glint.

For the turbid coastal environment, the water leaving radiances in the $0.66 - 0.87 \mu\text{m}$ spectral range are typically not close to zero mainly because of scattering by suspended materials. Under these conditions, the channels in this spectral region have very limited use for the retrieval of information on atmospheric aerosols. Because both the Gordon and Fraser algorithms derive aerosol information from channels in the $0.66 - 0.87 \mu\text{m}$ spectral range, these algorithms cannot be easily adapted for the retrieval of water leaving radiances over coastal waters.

We started in 1997 the development of an atmospheric correction algorithm for remote sensing of ocean color from hyperspectral imaging data acquired over coastal waters, after our development of the land versions of the atmosphere removal algorithm (ATREM) codes (Gao et al., 1993; Gao and Davis, 1997). In view of the limitations of the multi-channel atmospheric correction algorithms, we have designed a different algorithm, which can use channels in longer wavelengths to derive aerosol information. AVIRIS data are used for testing during the algorithm development.

2.3 Instrument Characteristics

The HypsIRI VSWIR instrument is a push broom imaging spectrometer (Mourioulis et al., 2000; Ungar, 1997) covering the solar spectral region between 0.38 and 2.5 micron in 10 nm channels. It has an accurate 60 m pixel size and 19 days of revisiting time for global mapping of land and shallow waters. The major science

measurement characteristics of VSWIR are given in Table 1. The required signal to noise ratios (SNRs) at the benchmark radiances are shown in Figure 2.

Table 1. Major HypsIRI VSWIR science measurement characteristics.

Spectral	
Range	380 to 2500 nm in the solar reflected spectrum
Sampling	≤ 10 nm {uniform over range}
Response	≤ 1.2 X sampling (FWHM) {uniform over range}
Accuracy	<0.5 nm
Radiometric	
Range & Sampling	0 to 1.5 X max benchmark radiance, 14 bits measured
Accuracy	$>95\%$ absolute radiometric, 98% on-orbit reflectance, 99.5% stability
Precision (SNR)	See Fig. 2 spectral plots at benchmark radiances
Linearity	$>99\%$ characterized to 0.1%
Polarization	$<2\%$ sensitivity, characterized to 0.5%
Scattered Light	$<1:200$ characterized to 0.1%
Spatial	
Range	>150 km (12 degrees at 700 km altitude)
Cross-Track Samples	>2500
Sampling	≤ 60 m
Response	≤ 1.2 X sampling (FWHM)
Uniformity	
Spectral Cross-Track	$>95\%$ cross-track uniformity { <0.5 nm min-max over swath}
Spectral-IFOV-Variation	$>95\%$ spectral IFOV uniformity { $<5\%$ variation over spectral range}
Temporal	
Orbit Crossing	11 am sun synchronous descending
Global Land Coast Repeat	19 days at equator
Rapid Response Revisit	3 days (cross-track pointing)
Sunglint Reduction	
Cross Track Pointing	4 degrees in backscatter direction
OnOrbit Calibration	
Lunar View	1 per month {radiometric}
Solar Cover Views	1 per day {radiometric}
Dark signal measurements	1 per orbit and edge detector tracking
Surface Cal Experiments	3 per year {spectral & radiometric}
Data Collection	
Land Coverage	Land surface above sea level excluding ice sheets
Water Coverage	Coastal zone -50 m and shallower
Solar Elevation	20 degrees or greater
Open Ocean/Ice Sheets	Averaged to 1km spatial sampling
Compression	≥ 3.0 lossless

(A)

(B)

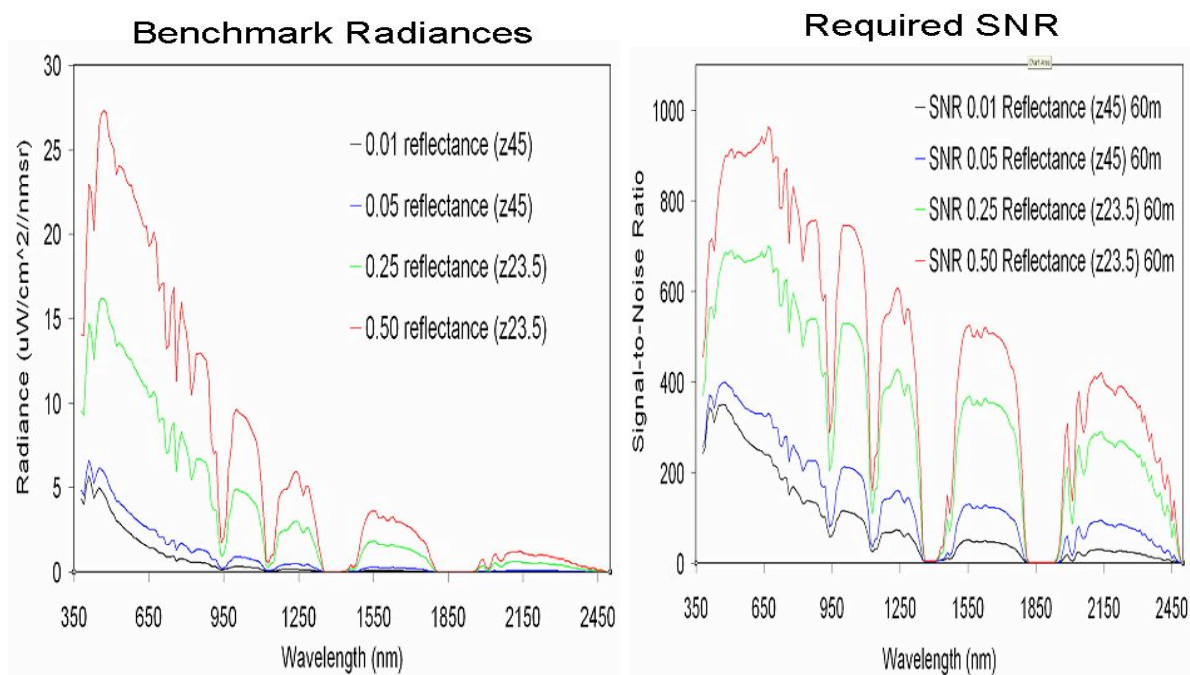


Fig. 2. Benchmark radiances (a) and the required signal to noise ratios (b).

Because the VSWIR instrument has sufficiently large dynamic range with 14 bits of digitization, all channels will not saturate over the brighter coastal waters, unlike the situation with the ocean color channels implemented on both the Terra and Aqua MODIS instruments. Several MODIS ocean color channels saturate over coastal waters (Gao et al., 2007). As a result, operational ocean color data products over coastal waters cannot be retrieved from radiances measured with MODIS ocean color channels. The saturation levels for MODIS ocean channels centered between 0.52 and 0.87 μm were originally specified too low. The same mistake was duplicated twice by Japanese researchers during their specifications of the Global Imager (GLI) (Nakajima et al., 1998) and a follow on instrument. Therefore, designers of satellite instruments should pay great attention to not only the signal to noise ratio requirements, but also the dynamic ranges.

The VSWIR spectral measurement has another important advantage, namely the data contain sufficient amount of information about atmospheric water vapor, aerosols, and thin cirrus clouds. It is possible to remove atmospheric effects from the VSWIR data themselves (Gao et al., 1993; Gao et al., 1998).

3 ALGORITHM DESCRIPTION

The proposed algorithm for retrieving the Level 2 water leaving reflectance data products from VSWIR Level 1b calibrated radiance data is described from both theoretical and practical point of view in this section.

3.1 Theoretical Description

3.1.1 Physics of the problem

The solar radiation on the sun-surface-sensor path is affected by absorption and scattering effects from atmospheric gases and aerosols. Accurate modeling of these effects is required in order to derive surface reflectance spectra from imaging spectrometer data. Among the approximately thirty atmospheric gases, only eight gases, namely water vapor (H₂O), carbon dioxide (CO₂), ozone (O₃), nitrous oxide (N₂O), carbon monoxide (CO), methane (CH₄), oxygen (O₂), and nitrogen dioxide (NO₂) produce observable absorption features in imaging spectrometer data over the range 0.4 to 2.5 μm with a spectral resolution between 1 and 20 nm. Figure 3 shows examples of simulated atmospheric transmittances for the eight gases. Approximately half of the spectral region between 0.4 and 2.5 μm is affected by atmospheric water vapor absorption. The absorption effects from the other seven gases are generally located in much narrower wavelength intervals.

Atmospheric gaseous molecules and aerosols scatter solar radiation. The short wavelength region between 0.4 and 0.7 μm is strongly affected by molecular scattering (Rayleigh scattering). Its effect decreases rapidly with increasing wavelength (λ^{-4}). The aerosol scattering effect also decreases with increasing wavelength, but at a slower rate (typically λ^{-2} to λ^{-1}).

3.1.2 Mathematical description of the algorithm

For atmospheric “window” channels where the absorption by atmospheric gases is negligible, the radiance (L_{obs}) of the ocean-atmosphere system measured by a satellite instrument can be expressed as (Fraser et al., 1997),

$$L_{obs} = L_o(\lambda; \theta, \phi; \theta_o, \phi_o; \tau_a) + L_{sfc}(\lambda; \theta, \phi; \theta_o, \phi_o; W; \tau_a) t'_u(\lambda; \theta; \tau_a) + L_w(\lambda; \theta, \phi; \theta_o, \phi_o; W; \tau_a; O) t_u(\lambda; \theta; \tau_a), \quad (1)$$

where L_o is the atmosphere-scattered radiance, if the radiance just above the sea surface were zero; L_{sfc} is the radiance of the light reflected from the surface; and L_w is the water-leaving radiance of light scattered from beneath the surface and penetrating it; t'_u is the upward transmittance through the atmosphere for the quantity L_{sfc} ; and t_u is the upward atmospheric transmittance for the quantity L_w . L_{sfc} includes the effects of specular

reflection by the air-water interfaces and the scattering effects by white caps.

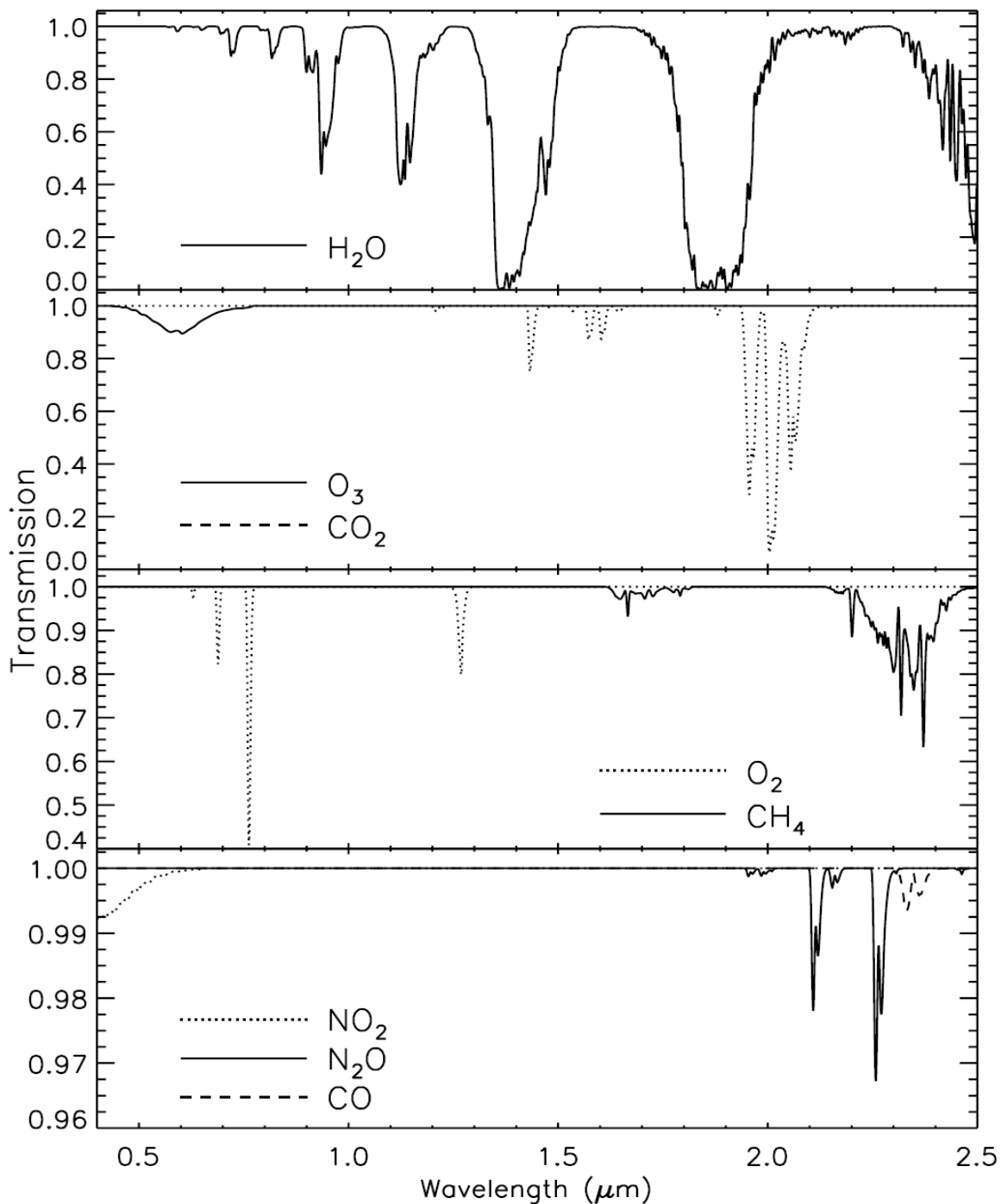


Fig. 3. Simulated transmittance spectra of atmospheric water vapor, carbon dioxide, ozone, nitrous oxide, carbon monoxide, methane, oxygen, and nitrogen dioxide.

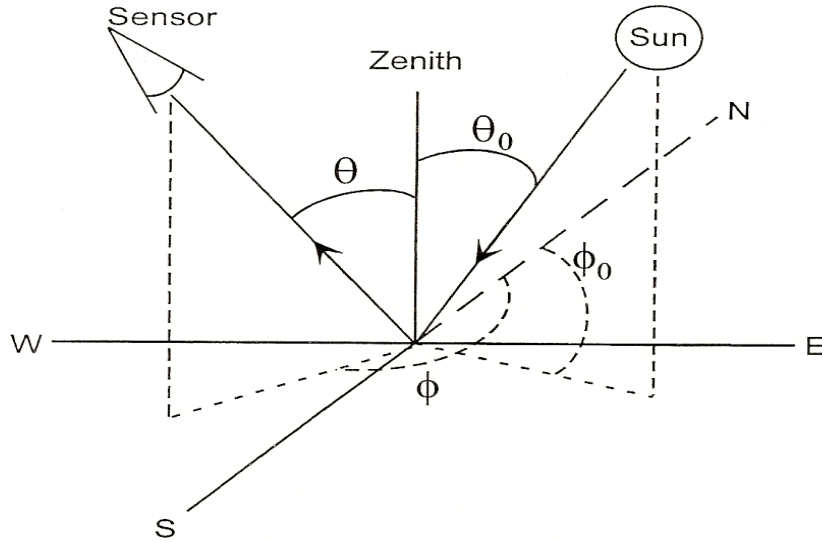


Fig. 4. Illustration for the definitions of solar zenith and azimuth angles and viewing zenith and azimuth angles.

The independent parameters in Eq. (1) are defined as follows:

- λ wavelength;
- θ, ϕ view zenith and azimuth angles from a spacecraft toward earth's surface;
- θ_0, ϕ_0 zenith and azimuth angles of the direct sunlight;
- W surface wind speed;
- τ_a atmospheric aerosol optical thickness;
- O a parameter representing the combined effects from all materials beneath the air-water interface.

Figure 4 illustrates the definitions of all the relevant angles. The definition of azimuth angles here follows the navigational convention. For convenience, we combine the first two terms in the right hand side of Eq. (1) as one term $L_{atm+sfc}$, i.e.,

$$L_{atm+sfc} = L_o(\lambda; \theta, \phi; \theta_0, \phi_0; \tau_a) + L_{sfc}(\lambda; \theta, \phi; \theta_0, \phi_0; W; \tau_a) t'_u(\lambda; \theta; \tau_a). \quad (2)$$

Substituting Eq. (2) into Eq. (1), we obtain,

$$L_{obs} = L_{atm+sfc} + L_w t_u. \quad (3)$$

We would like to follow the convention adopted in the 5S code (Tanre et al., 1990) to express radiances in reflectance units. Let's denote $\cos(\theta_o)$ as μ_o , and the downward solar irradiance at the top of the atmosphere when the solar zenith angle is equal to zero as E_o . By multiplying both sides of Eq. (3) by π and dividing them by $(\mu_o E_o)$, Eq. (3) becomes:

$$\pi L_{obs} / (\mu_o E_o) = \pi L_{atm+sfc} / (\mu_o E_o) + \pi L_w t_d t_u / (\mu_o E_o t_d), \quad (4)$$

where we have multiplied the numerator and denominator of the second term on the right side by the downward atmospheric transmittance t_d , which is the sum of the direct and diffuse downward transmittances of the sunlight through the atmosphere. We use several reflectances defined as

$$\rho_{obs}^* = \pi L_{obs} / (\mu_o E_o), \quad (5)$$

$$\rho_{atm+sfc}^* = \pi L_{atm+sfc} / (\mu_o E_o), \quad (6)$$

$$\rho_w = \pi L_w / (\mu_o E_o t_d) = \pi L_w / E_d = \pi R_{rs}, \quad (7)$$

where ρ_{obs}^* is the total apparent reflectance of the atmosphere-ocean system measured at the satellite level, $\rho_{atm+sfc}^*$ is the satellite level apparent reflectance resulting from the atmospheric scattering, specular reflection and white cap scattering at the air-water interface, ρ_w is the water leaving radiance in reflectance units, or simply the water leaving reflectance, E_d is the downward solar irradiance just above the surface, and R_{rs} is referred as the ‘‘remote sensing reflectance’’. It is equal to L_w / E_d and is widely used by the ocean color research community. ρ_w is equivalent to the quantity $[\rho_w]_N$ defined in Eq. (2) of Gordon (1997). By substituting Eqs. (5), (6), and (7) into Eq. (4), we obtain

$$\rho_{obs}^* = \rho_{atm+sfc}^* + \rho_w t_d t_u. \quad (8)$$

In order to take account of the effect of atmospheric reflection of upward water leaving radiances back to the surface, another factor of $1 / (1 - s \rho_w)$ needs to be multiplied to the second term in the right hand side of Eq. (8) (see Eqs. (11), (12), and (13) of Fraser et al. (1997)), where s is the reflectance of the atmosphere for isotropic radiance incident at its base. After inserting this factor, Eq. (8) becomes

$$\rho_{obs}^* = \rho_{atm+sfc}^* + \rho_w t_d t_u / (1 - s \rho_w) \quad (9)$$

For hyperspectral imaging data acquired from aircraft and satellite platforms and covering the 0.4 - 2.5 μm spectral region, more than half of the spectral region is affected by atmospheric gaseous absorption (Gao et al., 1993). We denote the total atmospheric gaseous transmittance on the Sun-surface-sensor path as T_g . We further assume that the atmospheric gaseous absorption process and the molecular and aerosol scattering process can be treated independently, i.e., we neglect the interaction term between gaseous absorption and molecular and aerosol scattering. After taking consideration of atmospheric gaseous absorption, Eq. (9) is modified as following:

$$\rho_{obs}^* = T_g [\rho_{atm+sfc}^* + \rho_w t_d t_u / (1 - s \rho_w)]. \quad (10)$$

Solving Eq. (10) for ρ_w yields

$$\rho_w = (\rho_{obs}^*/T_g - \rho_{atm+sfc}^*) / [t_d t_u + s (\rho_{obs}^*/T_g - \rho_{atm+sfc}^*)]. \quad (11)$$

Given a satellite measured radiance, the water leaving reflectance can be derived according to Eqs. (5) and (11) provided that the other quantities in the right hand side of Eq. (11) can be modeled theoretically.

Thin cirrus clouds frequently contaminate satellite measured images. Through analysis of the NASA JPL AVIRIS data, we have found that narrow channels located within the 1.38- and 1.88-micron atmospheric band centers are very effective in detecting thin cirrus clouds (Gao and Kaufman, 1995). Because the 1.38-micron channels are slightly affected by absorption from water vapor located above and within thin cirrus clouds, the water vapor effects must be removed in order to use the 1.38-micron channels for quantitative correction of thin cirrus effects in other channels (Gao et al., 1998; Gao et al., 2002). In the ATBD for the VSWIR land surface reflectance algorithm, we have already presented formulation for correction of thin cirrus effects. Basically, we assume that a homogeneous thin cirrus layer is located above a "virtual surface", which includes the effects of Rayleigh scattering and land or ocean surface reflection. The detailed techniques for thin cirrus detection and corrections have also been described by Gao et al. (1998) and Gao et al. (2002).

3.1.3 Algorithm implementations

The procedures described by Gao et al. (2000) for hyperspectral remote sensing of ocean color will be followed closely with the present VSWIR Level 2 water leaving reflectance algorithm. A spectrum-matching technique plus the use of pre-calculated lookup tables will be implemented in the VSWIR water leaving reflectance algorithm.

Lookup Tables

Because of the availability of the vector radiative transfer code from the Ahmad and Fraser (1982), the proper atmospheric layering structure in this code, and the treatment of wind-roughened water surfaces, we have decided to use a modified version of Ahmad and Fraser code (1982) to generate lookup tables used in our retrieving algorithm. More specifically, we use the code to generate the quantities $\rho_{atm+sfc}^*$, t_d , t_u , and s in Eq. (11). The code has been validated against other codes (Fraser et al., 1997). The same radiative transfer code has been used by Tanre et al. (1997) for remote sensing of aerosols from multi-channel imaging data acquired with the MODIS instruments (King et al., 1992; Salomonson et al., 1989) onboard the *Terra* and *Aqua* spacecrafts. In order to use the code to perform radiative transfer calculations, some input parameters, such as the vertical atmospheric temperature and pressure profiles, and aerosol models are required. The temperature and pressure profiles assumed are the U.S. Standard Model Atmosphere (1976). No gaseous absorption is included when generating the quantities $\rho_{atm+sfc}^*$, t_d , t_u , and s , which are related to scattering by atmospheric molecules and aerosols.

Aerosol models

The aerosol optical properties in the real coastal environment can vary significantly. In order to use the radiative transfer code to generate lookup tables, we have to assume sets of aerosol models. Following the approach of Gordon and Wang (1994), we have selected candidate aerosol models from those developed by Shettle and Fenn (1979). Most of the Shettle and Fenn models have two modes of particle size distributions – one small particle mode ($< 0.1 \mu\text{m}$) and one large particle mode ($> 0.3 \mu\text{m}$), except for the so called “tropospheric” aerosol models that have only the small particle size mode. The smaller size fraction of the particles is a mixture of 70% water soluble and 30% dust-like particles. The larger size fraction of the particles is made of sea-salt-based “oceanic” particles. The sizes of particles in both the small size mode and the large size mode can increase as the relative humidity of the atmosphere increases. The refractive indices of the particles also change as relative humidity changes (Shettle and Fenn, 1979). By mixing the small “tropospheric” particles with the large “oceanic” particles in different proportions, one can construct different types of aerosol models.

We have constructed four basic types of models. Table 2 lists the relative number concentrations of small and large particles for each type of the aerosol models. A small

change in the number of large particles in a given aerosol model can result in a significant change in the overall scattering property of the aerosol particles corresponding to the aerosol model. For each type of the aerosol models, we selected particle sizes corresponding to 5 relative humidities (RH) at 50%, 70%, 80%, 90%, and 98%. As a result, a total of 20 aerosol models have been selected. The aerosol models corresponding to RH = 80% are not included in the candidate aerosol models selected by Gordon and Wang (1994). However, these models are added to our selections based on suggestions by Eric P. Shettle of the Naval Research Laboratory. The reason behind our addition of candidate aerosol models is that the particle size changes drastically and non-linearly between relative humidity of 70% and 90% and the addition of aerosol models at 80% of RH is necessary.

Table 2: The relative number concentrations of small and large particles for four basic types of aerosol models.

Aerosol Type	Percent of small tropospheric particles by number	Percent of large "oceanic" particles by number
1 (Maritime)	99.0	1.0
2	99.5	0.5
3	99.8	0.2
4 (Tropospheric)	100.	0.0

Computations of aerosol-related lookup tables

Four lookup tables for the quantities $\rho_{atm+sfc}^*$, t_d , t_w , and s in Eq. (11) have been generated. The values of $\rho_{atm+sfc}^*$ in our lookup table are computed for the 20 aerosol models described above and for the following values of independent variables:

$$\begin{aligned} \lambda & 0.39, 0.41, 0.44, 0.47, 0.51, 0.55, 0.61, 0.67, 0.75, 0.865, 1.04, \\ & 1.24, 1.64, 2.25 \mu\text{m}; \\ \tau_a & 0, 0.1, 0.2, 0.3, 0.5, 0.7, 1.0, 1.3, 1.6, \text{ and } 2.0 \text{ at } 0.55 \mu\text{m}; \\ \theta_0 & 1.5, 12, 24, 36, 48, 54, 60, 66, \text{ and } 72 \text{ degrees}; \end{aligned}$$

θ 0, 1.5, 6, 12, 18, 24, 30, 36, 42, 48, 54, 60, 66, 72, 78, 84, and 88.5 degrees;

ϕ_0 0;

ϕ 0, 12, 24, 36, 48, 60, 72, 84, 90, 96, 108, 120, 132, 144, 156, 168, and 180 degrees;

W 2, 6, and 10 m/s;

O 0.

where the τ_a values are aerosol optical depths at $0.55 \mu\text{m}$. The grids of independent variables we selected for computing are, in most cases, sufficient for interpolation later. When calculating the quantity $\rho_{atm+sfc}^*$ using the modified version of Ahmad and Fraser code, we assume that the water leaving radiance at the bottom boundary is zero, and we include the effects of specular reflection at the air-water interface and the scattering by white caps (Fraser et al., 1997). When computing the other quantities (t_d , t_u , and s), we assume that the atmosphere is bounded by a Lambertian surface with zero reflectances at the bottom boundary.

Figure 5 shows examples of simulated $0.61\text{-}\mu\text{m}$ channel reflectance ($\rho_{atm+sfc}^*$) as a function of view angle for several relative azimuth angles. The simulations are made for a solar zenith angle of 36° , an aerosol optical depth of 0.2 at $0.55 \mu\text{m}$, the maritime aerosol model with a relative humidity of 80%, and a surface wind speed of 6 m/s. It is seen from this figure that for measurements within the solar plane and in the anti-solar side of the half plane ($\Delta\phi = 180$), the specular reflection from the wind-roughened water surface facets contribute significantly to $\rho_{atm+sfc}^*$ for the view zenith angles between 60° and 25° . As the relative azimuth angle decreases in the anti-solar side of the half plane, the specular reflection effects decrease. The specular reflection effect becomes zero for $\Delta\phi = 90^\circ$ (i.e., when the measurements are made in the plane perpendicular to the solar plane).

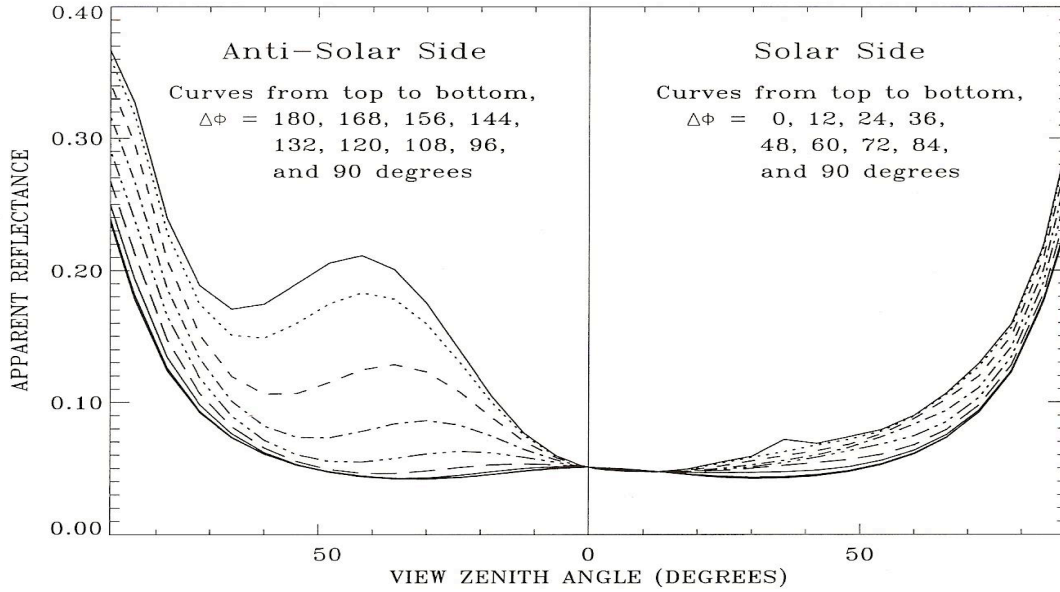


Fig. 5. Examples of simulated 0.61- μm channel reflectance ($\rho^*_{atm+sfc}$) as a function of view angle for several relative azimuth angles. The simulations are made for a solar zenith angle of 36° , an aerosol optical depth of 0.2 at $0.55 \mu\text{m}$, the maritime aerosol model with a relative humidity of 80%, and a surface wind speed of 6 m/s.

Figure 6 shows examples of simulated reflectances ($\rho^*_{atm+sfc}$) as a function of wavelength for the four types of aerosol models listed in Table 2 at a same relative humidity of 50%. The simulations are made for a solar zenith angle of 36° , a view zenith angle of 54° , a relative azimuth angle of 156° , an aerosol optical depth of 0.7 at $0.55 \mu\text{m}$, and a surface wind speed of 6 m/s. For the 1st type of aerosol model (maritime aerosol model) with most of large “oceanic” particles, the reflectance spectrum is most flat in the $0.4 - 2.25 \mu\text{m}$ spectral region. As the number of large particles decreases, the reflectances decrease more rapidly with increasing wavelengths. The spectral slopes for the four curves change most rapidly in the $0.4 - 0.9 \mu\text{m}$ wavelength interval. This indicates that the spectra in the $0.4 - 0.9 \mu\text{m}$ region contain most of information on aerosol particle sizes. The spectral slopes for the four curves also change (though less rapidly) with wavelengths in the $1.0 - 2.25 \mu\text{m}$ region. This indicates that the spectra in the $1.0 - 2.25 \mu\text{m}$ region also contain some information about particle sizes.

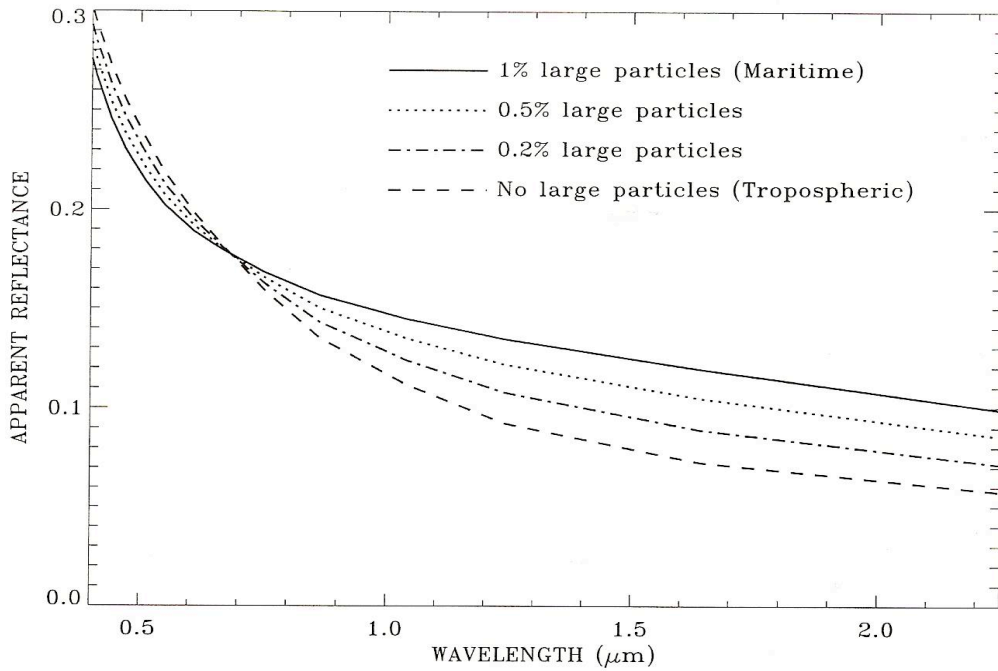


Fig. 6. Examples of simulated reflectances ($\rho_{atm+sfc}^*$) as a function of wavelength for four types of aerosol models at the same relative humidity of 50%. The simulations are made for a solar zenith angle of 36° , a view zenith angle of 54° , a relative azimuth angle of 156° , an aerosol optical depth of 0.7 at $0.55 \mu\text{m}$, and a surface wind speed of 6 m/s.

For the turbid coastal environment where the water leaving radiances for channels with $\lambda < 0.9 \mu\text{m}$ are often not close to zero, these channels are not very useful for estimating particle sizes. Because the water leaving radiances for channels above $1 \mu\text{m}$ are more close to zero for the coastal waters and because the $1.0 - 2.25 \mu\text{m}$ region also contains information about aerosol particle sizes, it is justified to use channels in the $1.0 - 2.25 \mu\text{m}$ spectral region to estimate aerosol particle sizes from remotely sensed data acquired over coastal waters.

Calculation of gas transmittances

As shown in Fig. 1b, major atmospheric absorption bands are seen in measured spectra. A fast line-by-line-based module for calculating atmospheric gaseous transmittances has previously been developed in the land version of ATREM code (Gao and Davis, 1997). In this module, high resolution atmospheric gaseous transmittance

spectra are calculated with the use of a large database (~150 megabytes) containing pre-calculated high resolution (0.05 cm^{-1}) absorption coefficients for six atmospheric gases (H_2O , CO_2 , N_2O , CO , CH_4 , and O_2). The database was generated using a line-by-line code developed by W. Ridgway (personal communication, 1996). The high resolution spectra are smoothed to medium resolution spectra ($\sim 0.2 \text{ nm}$) and merged with a medium resolution ozone transmittance spectrum ($\sim 0.2 \text{ nm}$). The transmittances for ozone and nitrogen dioxide are calculated based on their absorption cross sections. The medium resolution spectra are further smoothed to lower resolution to match the resolutions of instruments, such as those of AVIRIS. This module is ported over to our ocean color version of the atmosphere removal algorithm.

Steps for practical retrievals

At present, the retrievals of water leaving reflectances from measured hyperspectral imaging data cubes (two spatial dimensions and one spectral dimension) are made on a pixel-by-pixel basis. A spectral matching technique is used in the retrievals. The steps involved in the retrievals are listed below.

- (a). The solar zenith and azimuth angles are derived based on the date and time of the data acquisition and on the latitude and longitude of the scene. The view zenith and azimuth angles are known.
- (b). The 2-way atmospheric gaseous transmittance spectra, T_s , which match the spectral resolutions of all channels in an imaging spectrometer and correspond to the Sun-surface-sensor path, are calculated using the method described above. A total of 60 transmittance spectra corresponding to vertical column water vapor amounts ranging from 0 to 15 cm are calculated. This range of column water vapor amounts covers typical atmospheric conditions in which column water vapor amounts range from about 0.4 cm to 4.3 cm. In order to get spectra corresponding to different water vapor amounts, the water vapor vertical profile is scaled by different factors during the calculations. The transmittance spectra are stored in a lookup table.
- (c). A measured radiance spectrum is divided by the solar irradiance curve above the atmosphere to obtain the apparent reflectance spectrum (see Eq. (5)).
- (d). A water vapor amount is estimated from the $0.94\text{-}\mu\text{m}$ and the $1.14\text{-}\mu\text{m}$ water vapor bands in the apparent reflectance spectrum using a 3-channel ratioing technique and a procedure to search the table containing the 60 gaseous transmittance spectra (Gao

et al., 1993). Based on the estimated water vapor value and the use of the lookup table procedure again, the best estimation of gaseous transmittance spectrum corresponding to the measured spectrum is obtained.

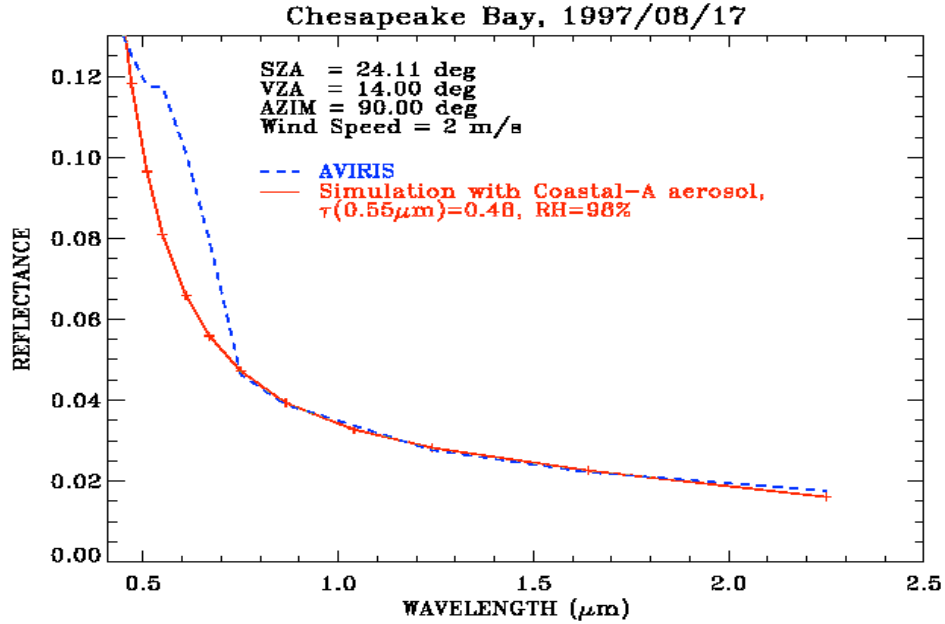


Fig. 7. An example of spectrum-matching for the derivation of water leaving reflectances. The differences between the two lines in the visible are proportional to water leaving reflectances.

(e). The apparent reflectance spectrum is divided by the estimated gaseous transmittance spectrum to obtain the spectrum of ρ_{obs}^*/T_g (see Eq. (11)). The values of ρ_{obs}^*/T_g corresponding to the 14 wavelengths in our tables for scattering quantities are obtained from the spectrum of ρ_{obs}^*/T_g through linear interpolation. The 14 values of ρ_{obs}^*/T_g are used in our retrieval of an aerosol model and an optical depth using a spectrum-matching technique. Figure 7 shows an example of spectrum matching using AVIRIS data. The dashed line is derived from the AVIRIS “measured” data. In this case of spectral matching, the channels at 1.04, 1.24, 1.64 and 2.25 μm are assigned a weighting factor of 1, while all the other channels short of 1 μm are assigned a weighting factor of 0. The measured data for the four channels at 1.04, 1.24, 1.64 and 2.25 μm are compared with the $\rho_{atm+sfc}^*$ data stored in a pre-computed lookup table for each of the 20 aerosol models and for each of the 10 optical depths. The solid line is the curve of $\rho_{atm+sfc}^*$ versus wavelength corresponding to our best

estimates of the aerosol model and optical depth. The dashed curve and the solid curve agree quite well for wavelengths greater than 0.86 μm . The differences between the dashed curve and the solid curve near the 0.55 μm (green) spectral region are attributed to water leaving radiances in the visible.

- (f). The values of the quantities ρ_{atm+sf}^* , t_d , t_u , and s at the wavelength grids of an imaging spectrometer are determined through interpolations and extrapolations from the corresponding values at the 14 wavelengths determined in step (e), and the water leaving reflectance spectrum is derived according to Eq. (11).

3.1.4 Descriptions of input and output data

The VSWIR Level 2 water leaving reflectance algorithm requires input data sets from the standard VSWIR L1b calibrated radiance data cubes and associated ancillary data. The radiance data cubes can be stored in three formats: BSQ (band sequential), BIL (band interleave by line), and BIP (band interleave by pixel). The most preferred format is BIL, the natural format of push broom imaging spectrometers. The inputs from ancillary data are solar zenith angle, solar azimuth angle, view zenith angle, view azimuth, and surface elevation. Optional input data include column atmospheric ozone and nitrogen dioxide amounts. Default values based on climatology will be used if the optional input data are not available.

The output VSWIR Level 2 data sets include water leaving reflectance data cubes in any one of the three formats (BSQ, BIL, BIP), aerosol optical depth images, and quality assurance (QA) parameter images. The QA parameters can contain a variety of information about each pixel and the corresponding data processing stream. We intend to use short integers (I^*2 , 16 bits) to store the QA parameters.

3.1.5 Variance and uncertainty estimates

There are a number of sources of errors in water leaving reflectance retrievals from imaging spectrometer data. The sources include but not limited to:

1. Uncertainty in the sensor calibration.
2. Uncertainty in the atmospheric radiative transfer codes.
3. Uncertainty in the vertical atmospheric temperature and moisture profiles.
4. Lacking of absorbing aerosol models and dust models in the lookup tables.
5. Inability in proper determination of aerosol models and optical depths, particularly for absorbing aerosols from measured imaging spectrometer data.

6. Uncertainty in removal of sunglint effects from high spatial resolution images.

Absorbing aerosols and residual sunglint effects can introduce large errors in the derived water leaving reflectance spectra from VSWIR data. Mis-treating thin cirrus clouds as aerosols will not introduce significant errors in the retrieved water leaving reflectance in the visible. However, it will generate an incorrect aerosol climatology over the ocean, which is the case for the SeaWiFS ocean aerosol product.

3.2 Practical Considerations

Considerations of numerical computation, programming, and exception handling are presented in this section.

3.2.1 Numerical computation considerations

Problems with numerical stability and round-off errors are not expected with this algorithm.

3.2.2 Programming/procedural considerations

In the present implementation of ocean version of the ATREM code, a total of 60 gaseous transmittance spectra for different water vapor amounts are calculated for each scene and stored on memory for internal use during the retrieval of surface reflectance spectra for the scene. The simulation of the 60 spectra that match the wavelengths and spectral resolution of a given imaging spectrometer takes quite a bit of CPU time. We plan to modify the code so that the 60 spectra are calculated only once for each spectrometer, and save the spectra onto hard disks for later use.

4 SAMPLE RESULTS

Water leaving reflectances have been derived from AVIRIS and other imaging spectrometer data over the past decade with our atmospheric correction algorithms. Sample results are presented in this section.

Figure 8 shows a set of images processed from an AVIRIS data set acquired over the Chesapeake Bay area in late 1990s. The 0.66- μm image shows clearly features in the water resulting from backscattering by suspended materials in the water. As the wavelength increases, the features in water are seen less clearly. This is the reason that we have used only channels at wavelengths greater than 1 μm in many cases for the derivation of aerosol information from AVIRIS data during retrievals. Figure 9a shows two radiance spectra – one measured over a very turbid area (solid line) and one over a less turbid area (dotted line) from a different AVIRIS scene, but also over the

Chesapeake Bay area. Figure 9b shows the water leaving reflectance spectra retrieved from the two radiance spectra in Fig. 9a. The overall shapes of the reflectance spectra above $0.45 \mu\text{m}$ are quite consistent with those measured from other field measurements (e.g., Lee et al., 1996; Han and Rundquist, 1997). Below $0.45 \mu\text{m}$, the reflectances fall off too rapidly with decreasing wavelengths and even become negative for wavelengths less than about $0.41 \mu\text{m}$. This problem has been observed for other AVIRIS scenes (Carder et al., 1993; Hamilton et al., 1993). It is likely due to radiometric calibration of AVIRIS instrument, which reports too small radiances in the blue spectral region. We do not have field-measured reflectance spectra corresponding to the two spectra in Fig. 9b. Therefore, it is not possible in this case to have direct comparisons between the retrieved reflectance spectra and field-measured reflectance spectra.

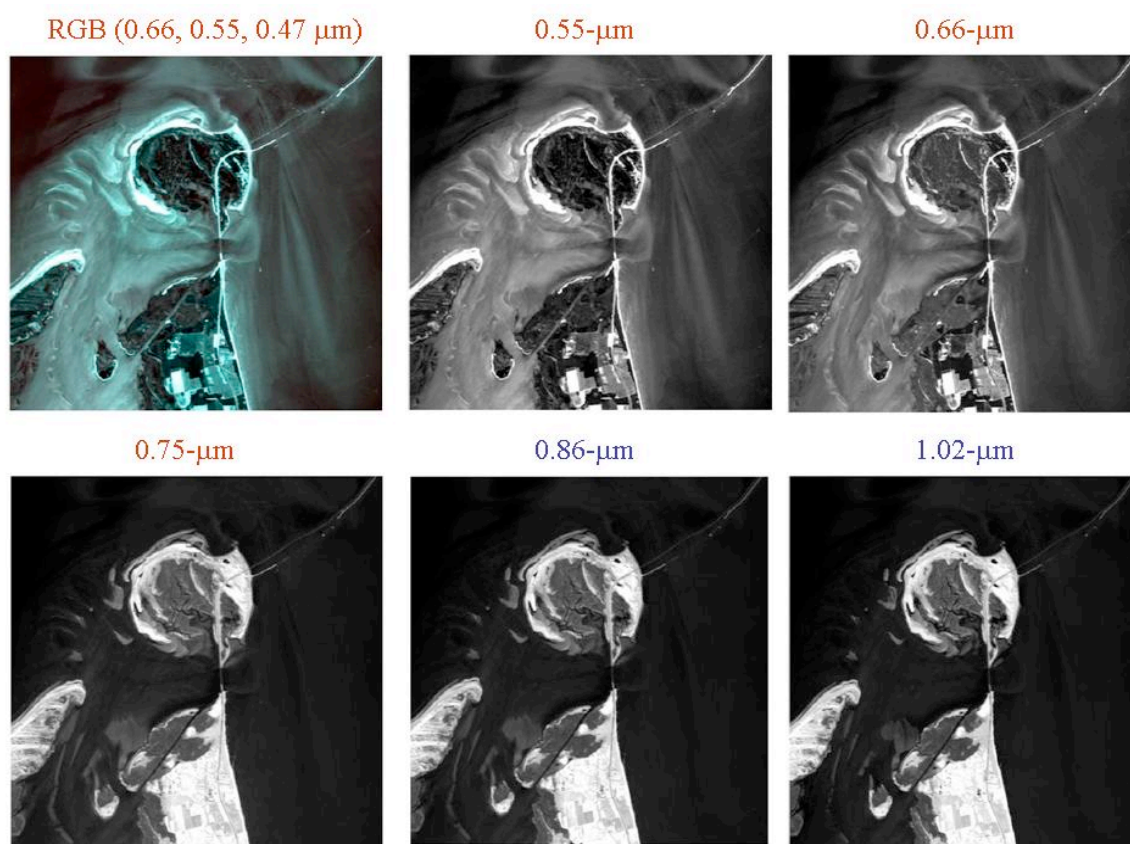


Fig. 8. A set of images processed from an AVIRIS data set acquired over the Chesapeake Bay area in late 1990s. As wavelength increases, the corresponding image over turbid water areas becomes increasingly darker.

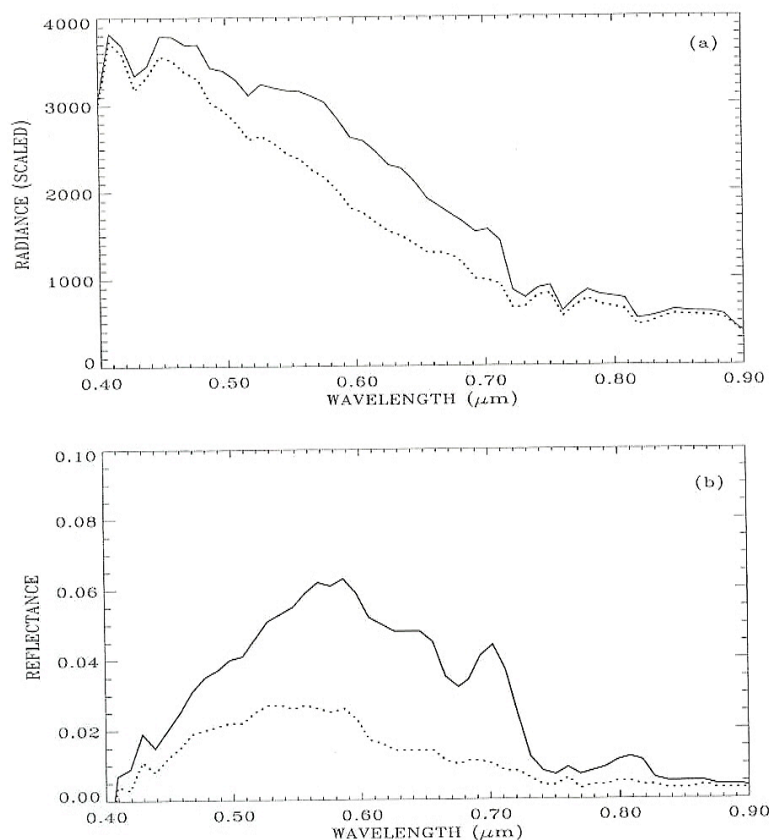


Fig. 9. (a) – AVIRIS radiance spectra measured over a very turbid water area (solid line) and a less turbid area (dotted line), and (b) - the water leaving reflectance spectra retrieved from the two radiance spectra in (a).

The results of water leaving reflectance retrievals from an AVIRIS data set acquired over the Florida Keys ($24^{\circ} 36' \text{ N}$ and $81^{\circ} 47' \text{ W}$) in the spring of 1996 are present in Figure 10. In Fig. 10a we show a color composite image of the scene. The image covers an area of approximately 50 km by 11 km. During the processing of this color image, the 0.70- μm AVIRIS channel is assigned as the red channel, the 0.55- μm channel as the green channel, and the 0.44- μm channel as the blue channel. The water is quite clear over the scene. It becomes increasingly shallow from the upper left part of the scene to the lower right part of the scene. Reflection off the bright calcium carbonate sand bottom increasingly dominates the measured spectra in the visible spectral region over shallower water areas. Figure 10b shows the radiance spectra extracted from the four areas marked as I, II, III, and IV in the Fig. 10a image. Fig. 10c shows our retrieved water leaving reflectance spectra. For the deepest water reflectance spectrum (marked with a symbol "I"), the reflectance peak is centered near 0.50 μm . As the water depth

decreases, the reflectance peak shifts toward longer wavelengths. For the shallowest water (marked with a symbol "IV"), the reflectance peak is centered approximately at $0.57 \mu\text{m}$. The shapes of the Fig. 10c reflectance spectra above $0.45 \mu\text{m}$ are consistent with those of field-measured reflectance spectra over similar clear waters with a sand bottom in Lake Tahoe (Hamilton et al., 1993). Again, we do not have field-measured reflectance spectra corresponding to the four spectra in Fig. 10c for direct comparisons between the retrieved reflectances and field-measured reflectances.

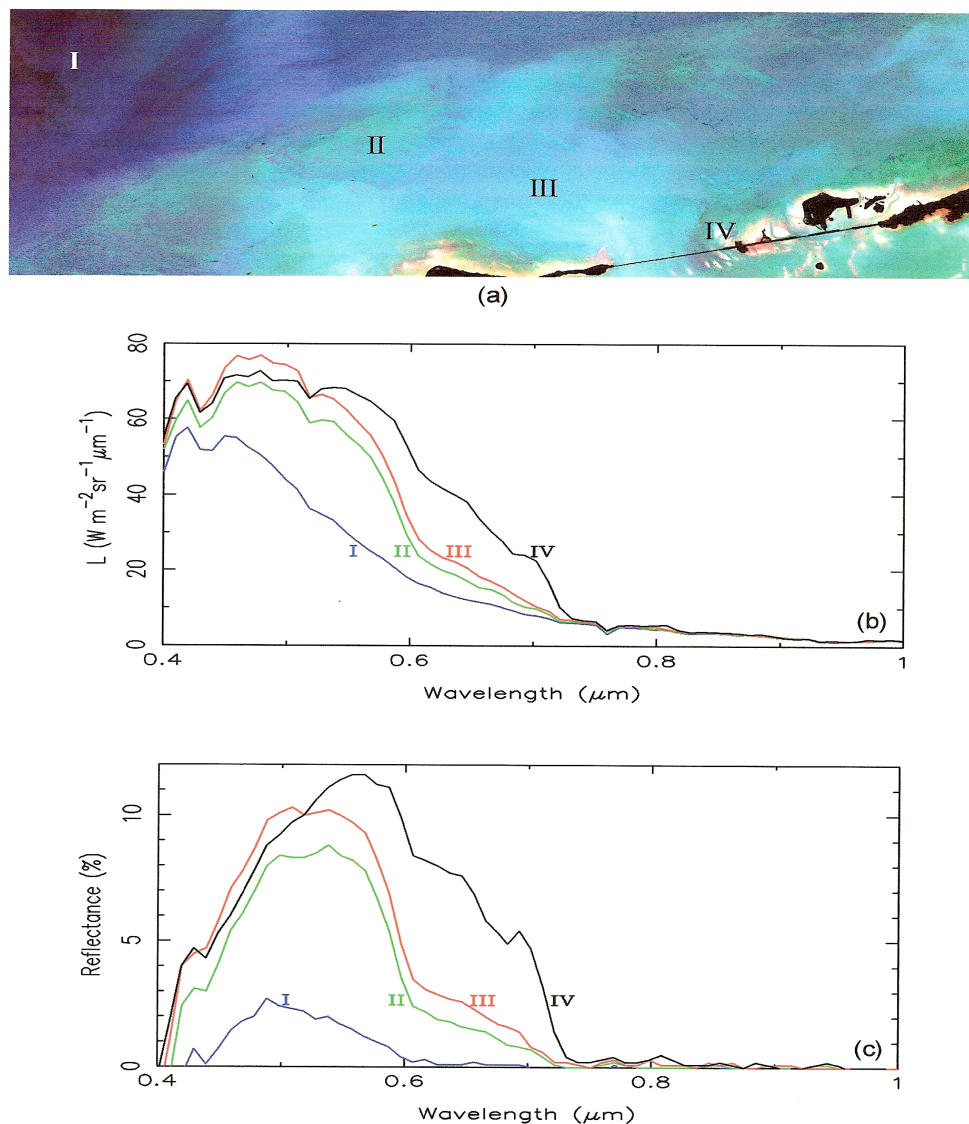


Fig. 10. (a) – a color composite image of the AVIRIS scene over Florida Keys, (b) – the radiance spectra extracted from the four areas marked as I, II, III, and IV in (a), and (c) – the retrieved water leaving reflectance spectra from the four spectra in (b).

Figure 11 shows comparisons between water leaving reflectance retrievals from a 1996 AVIRIS data set and a 2002 Hyperion data set containing sandy areas under shallow waters. The shapes of water leaving reflectance spectra retrieved from the two data sets are very similar. A small local reflectance maximum near 0.81 micron, due to local minimum liquid water absorption, is observed in both spectra.

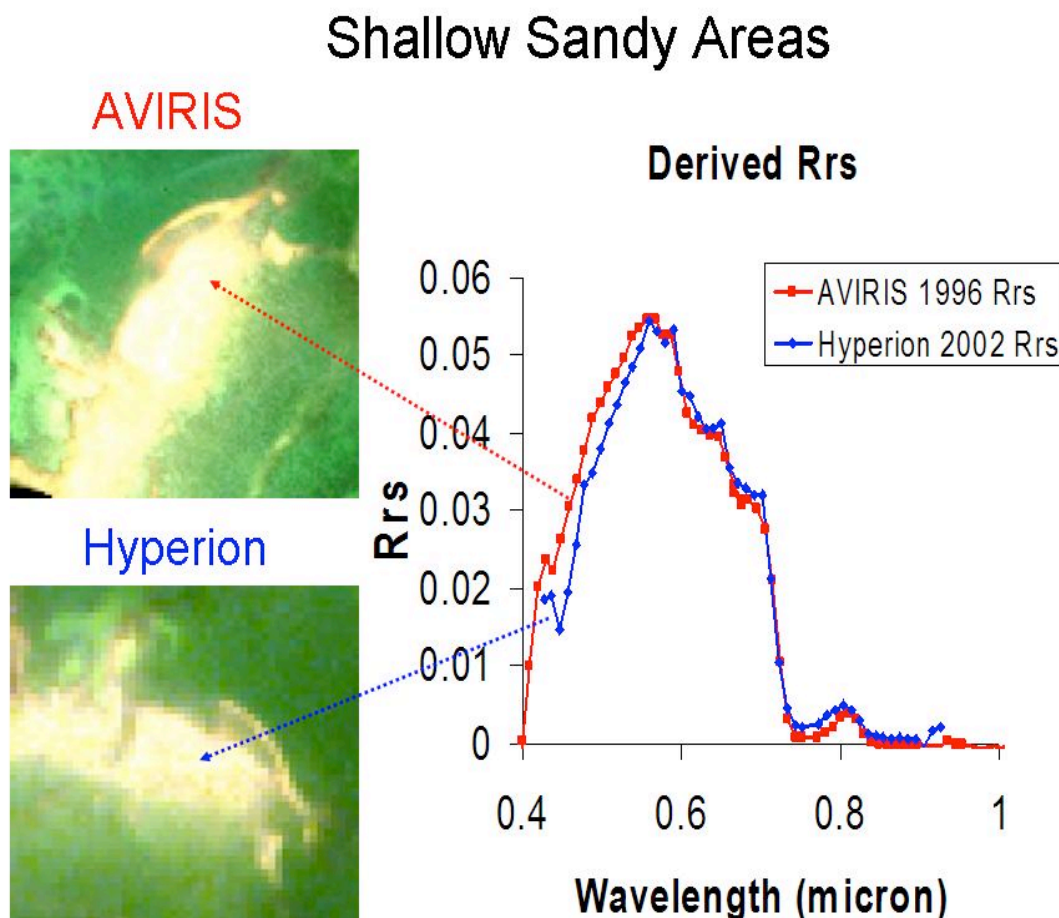


Fig. 11. Examples of water leaving reflectance retrievals from AVIRIS and Hyperion data sets covering the same shallow water areas.

One concern by the HypsIRI Science Study Groups in remote sensing of water surfaces using VSWIR measurements is the sunglint effect, i.e., the light specularly reflected from the water surface and never penetrated into water. Without adequate corrections of the sunglint effect, significant errors will be present in the retrieved water leaving reflectances. We have made preliminary investigations on sunglint removals from existing AVIRIS data sets using our atmospheric correction algorithms.

The left plot in Fig. 12 shows one AVIRIS image acquired over Hawaii in the spring of 2000. The sunglint effects are observed in most portions of the image, particularly the upper right portion. Fig. 13 shows a sample apparent reflectance spectrum (see Eq. (5) for definition) over a sunglint pixel. Sunglint contributes a nearly constant reflectance value of approximately 8% in narrow atmospheric “window” regions around 0.86, 1.04, 1.24, 1.64, and 2.25 μm . Because individual wave facets are observed in the high spatial resolution (~ 20 m) AVIRIS image, it is not possible to predict the sunglint contributions to reflectances on a pixel-by-pixel basis using the well known Cox and Munk (1954) model. As a result, our ocean version of the ATREM code (Gao et al., 2000) is not quite suited for atmospheric and sunglint corrections for the AVIRIS scene as shown in the left plot of Fig. 12. In view of the nearly spectrally flat sunglint contributions to the apparent reflectance spectra and the difficulties in predicting sunglint effects on a pixel-by-pixel basis using the Cox and Munk model, we have decided to first make a correction to the Rayleigh scattering effect and to get a reflectance data cube, which still contains the sunglint effects. For each pixel, we compute a mean reflectance value of three AVIRIS channels near 1.03 μm and then subtract out the mean value for every channel in the spectrum to get the “glint-removed” water leaving reflectance spectrum. The right plot in Fig. 12 shows the glint-removed RGB image. By comparing the two images in Fig. 12, it is seen that the glint effects are effectively removed with our empirical technique. The spatial distribution patterns of underwater features in the right plot (after glint correction) are observed much better than those in the left plot (before glint correction).

First Case of Glint Removal Using AVIRIS Data Over Hawaii Waters

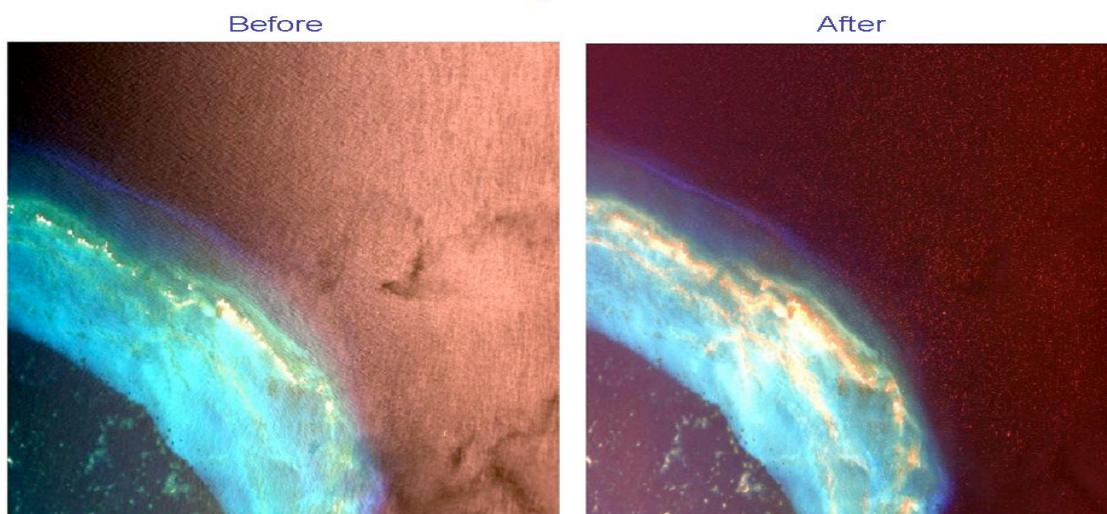


Fig. 12. An example of AVIRIS image before (left plot) and after (right plot) glint removal with our empirical technique.

An AVIRIS Apparent Reflectance Spectrum
(with Sunlint Effects)_

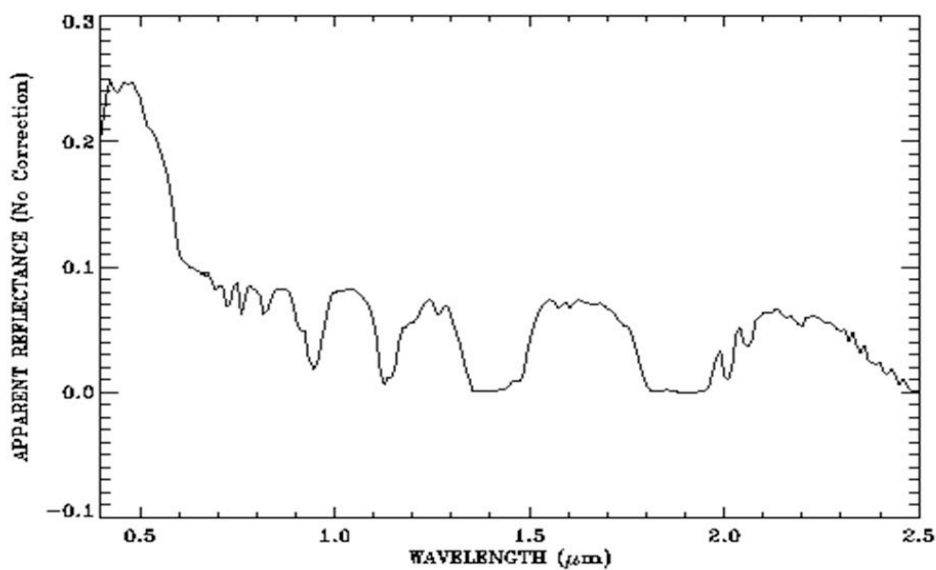


Fig. 13. An example of AVIRIS apparent reflectance spectrum with sunlint effects.

Second Case of Glint Removal Using AVIRIS Data Over Pearl Harbor, HI



Fig. 14. An example of AVIRIS image over Pearl Harbor, Hawaii before (left plot) and after (right plot) glint removal with our empirical technique.

Figure 14 shows the second case of glint removal from an AVIRIS data set acquired over Pearl Harbor in the spring of 2000. The waving patterns seen in the left plot are

removed completely in the right plot. Figure 15 shows the third case of glint removal from an AVIRIS data set acquired over Kaneohe Bay, Hawaii in the spring of 2000. Images and sample spectra before and after glint corrections are all presented. Waving patterns seen in the left image are removed completely in the right plot image. The underwater coral spatial distribution patterns are seen much better in the right plot image than in the left plot image. The three case studies demonstrate that our empirical technique is very effective in removing most of the sunglint effects from AVIRIS data sets. More research is needed to assess the accuracy of the technique for glint removals.

Third Case of Glint Removal Using AVIRIS Data Over Kaneohe Bay, HI

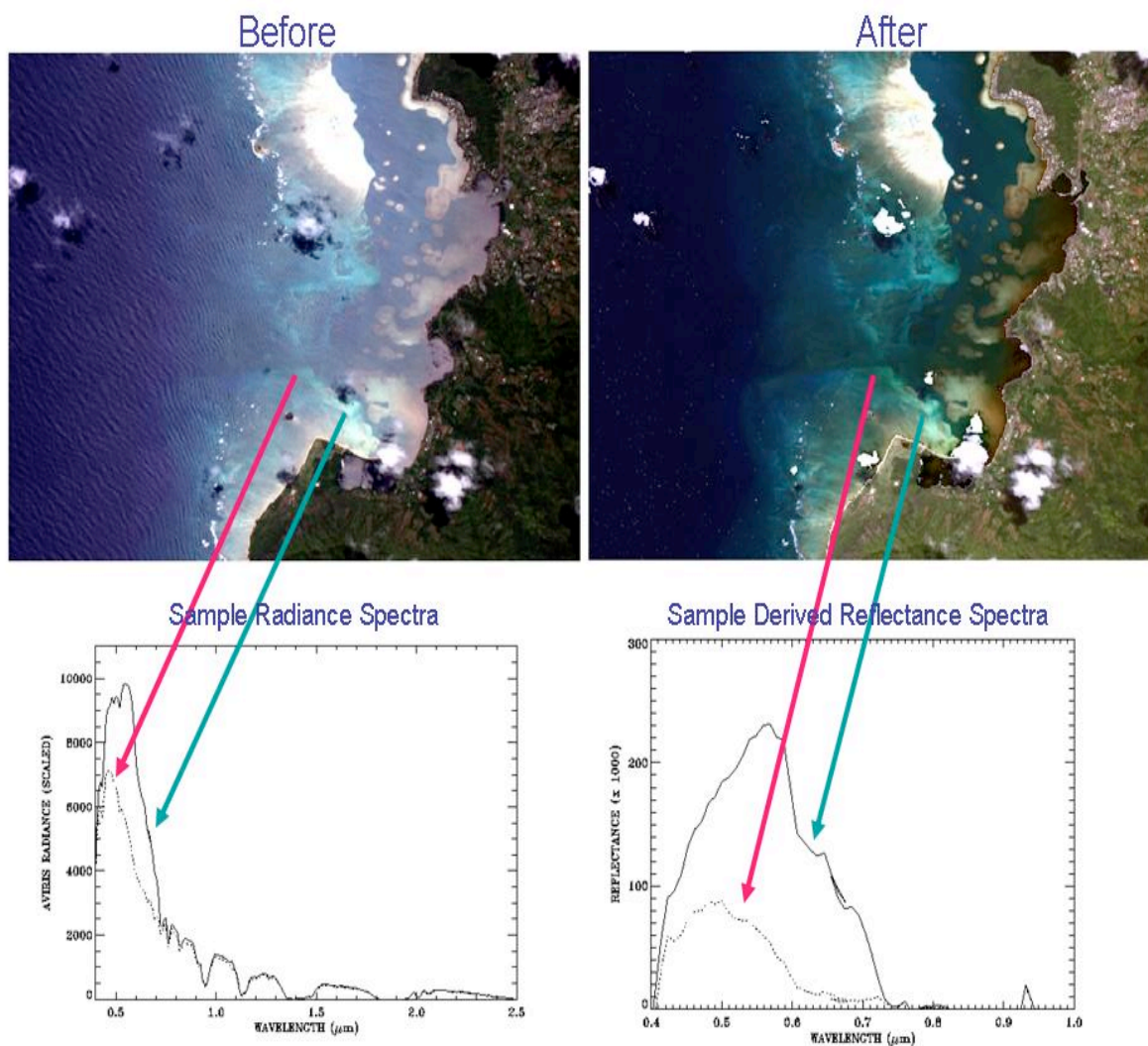


Fig. 15. An example of AVIRIS image over Kaneohe Bay, Hawaii before (left plot) and after (right plot) glint removal with our empirical technique. Images and sample spectra before and after sunglint removal are all presented.

5 RESEARCH AGENDA

At present, our lookup tables have been built for 20 aerosol models. Such lookup tables are adequate for retrievals of water leaving reflectances from remotely sensed data acquired under typical atmospheric conditions. Additional aerosol models, such as models for Sahara dust and Asian dust, need to be included into our lookup tables. Through analysis of the Aqua MODIS data, we have found that the aerosols in summer months in the Chesapeake Bay areas in eastern US are more absorbing than in other months. The time-dependent aerosol models also need to be developed and included into our lookup tables in the future.

We have occasionally observed from other AVIRIS data sets acquired over coastal environments that the water leaving radiances for channels above 1 μm for some pixels are not close to zero; such as the situation when large amount of material is floating on the water surface. The derivation of aerosol information on aerosols from these pixels is not possible. Under this situation, we can use aerosol information derived from other pixels where the water leaving radiances above 1 μm are close to zero, and extrapolate the aerosol information to these pixels when deriving water leaving reflectances over these pixels.

6 REFERENCES

- Ahmad, Z., and Fraser, R. S. (1982). An iterative radiative transfer code for ocean-atmosphere systems, *Journal of Atmospheric Science*, 39, 656-665.
- Carder, K. L., Reinersman, P., Chen, R. F., Muller-Karger, F., Davis, C. O., and Hamilton, M. (1993). AVIRIS calibration and application in coastal oceanic environments, *Remote Sens. Env.*, 44, 205-216.
- Cox, C., and Munk, W. (1954). Measurement of the roughness of the sea surface from photographs of the Sun's glitter, *J. Opt. Soc. America*, 44, 838-850.
- Davis, C. O., Bowles, J., Leathers, R. A., Korwan, D., Downes, T. V., Snyder, W. A., Rhea, W. J., Chen, W., Fisher, J., Bissett, W. P., & Reisse, R. A. (2002). Ocean PHILLS hyperspectral imager: design, characterization, and calibration, *Optics Express*, 10, 210-221.

- Fraser, R. S., Mattoo, S., Yeh, E.-N., & McClain, C. R. (1997). Algorithm for atmospheric and glint corrections of satellite measurements of ocean pigment, *Journal of Geophysical Research*, 102, 17107-17118.
- Gao, B.-C., Heidebrecht, K. B., & Goetz, A. F. H. (1993). Derivation of scaled surface reflectances from AVIRIS data, *Remote Sensing of Environment*, 44, 165-178.
- Gao, B.-C., and Kaufman, Y. J. (1995). Selection of the 1.375- μm MODIS channel for remote sensing of cirrus clouds and stratospheric aerosols from space, *J. Atm. Sci.*, 52, 4231-4237.
- Gao, B.-C., & Davis, C. O. (1997). Development of a line-by-line-based atmosphere removal algorithm for airborne and spaceborne imaging spectrometers, in *SPIE Proceedings*, 3118, 132-141.
- Gao, B.-C., et al. (1998). Correction of thin cirrus path radiance in the 0.4 - 1.0 μm spectral region using the sensitive 1.375- μm cirrus detecting channel, *J. Geophys. Res.*, 103, 32169-32176.
- Gao, B.-C., Montes, M. J., Ahmad, Z., & Davis, C. O. (2000). Atmospheric correction algorithm for hyperspectral remote sensing of ocean color from space, *Applied Optics*, 39, 887-896.
- Gao, B.-C., Yang, P., Han, W., Li, R.-R., and Wiscombe, W. J. (2002). An algorithm using visible and 1.38-micron channels to retrieve cirrus cloud reflectances from aircraft and satellite data, *IEEE Trans. Geosci. Remote Sensing*, 40, 1659 – 1668.
- Gao, B.-C., Montes, M. J., Li, R.-R., Dierssen, H. M., and Davis, C. O. (2007). An atmospheric correction algorithm for remote sensing of bright coastal waters using MODIS land and ocean channels in the solar spectral region, *IEEE Tran. Geosc. Remote Sensing*, 45, 1835-1843.
- Goetz, A. F. H., Vane, G., Solomon, J., & Rock, B. N. (1985). Imaging spectrometry for Earth remote sensing, *Science*, 228, 1147–1153.
- Gordon, H. R. (1978). Removal of atmospheric effects from satellite imagery of the oceans, *Appl. Opt.*, 17, 1631-1636.

- Gordon, H. R., and Wang, M. (1994). Retrieval of water leaving radiance and aerosol optical thickness over the oceans with SeaWiFS: a preliminary algorithm, *Appl. Opt.*, 33, 443-452.
- Gordon, H. R. (1997). Atmospheric correction of ocean color imagery in the Earth Observing system era, *J. Geophys. Res.*, 102, 17081-17106.
- Green, R. O., Eastwood, M. L., Sarture, C. M., Chrien, T. G., Aronsson, M., Chippendale, B. J., Faust, J. A., Parvi, B. E., Chovit, C. J., Solis, M., Olah, M. R., & Williams, O. (1998). Imaging spectrometry and the Airborne Visible/Infrared Imaging Spectrometer (AVIRIS), *Remote Sensing of Environment*, 65, 227-248.
- Hamilton, M., et al. (1993). Estimating chlorophyll content and bathymetry of Lake Tahoe using AVIRIS data, *Remote Sens. Env.*, 44, 217-230.
- Han, L., and Rundquist, D. C. (1997). Comparison of NIR/RED ratio and first derivative of reflectance in estimating algal-chlorophyll concentration: A case study in turbid reservoir, *Remote Sens. Env.*, 62, 253-261.
- King, M. D., Kaufman, Y. J., Menzel, W. P., and Tanre, D. (1992). Remote sensing of cloud, aerosol, and water vapor properties from the Moderate Resolution Imaging Spectrometer (MODIS), *IEEE Trans. Geosci. Remote Sensing*, 30, 1-27.
- Lee, Z. P., et al. (1996). Method to derive ocean absorption coefficients from remote-sensing reflectance, *Appl. Opt.*, 35, 453-462.
- Mourioulis, P., Green, R. O., & Chrien, T. G. (2000). Design of pushbroom imaging spectrometers for optimum recovery of spectroscopic and spatial information, *Applied Optics*, 39, 2210-2220.
- Nakajima, T. Y., Nakajima, T., Nakajima, M., Fukushima, H., Kuji, M., Uchiyama, A., and Kishino, M. (1998). Optimization of the advanced earth observing satellite II Global imager channels by use radiative transfer calculations, *Applied Optics*, 37, 3149-3163.
- Salomonson, V. V., Barnes, W. L., Maymon, P. W., Montgomery, H. E., and Ostrow, H. (1989) MODIS: Advanced facility instrument for studies of the earth as a system, *IEEE Trans. Geosci. Remote Sens.*, 27, 145-153.

- Shettle, E. P., and Fenn, R. W. (1979). Models for the aerosols of the lower atmosphere and the effects of humidity variations on their optical properties, AFGL-TR 790214, 94 pp., Opt. Phys. Div., Air Force Geophys. Lab., Hanscom Air Force Base, Mass.
- Tanre, D., et al. (1990). Description of a computer code to simulate the satellite signal in the solar spectrum: the 5S code, *Int. J. Remote Sensing*, 11, 659-668.
- Tanre, D., et al. (1997). Remote sensing of aerosol properties over oceans using the MODIS/EOS spectral radiances, *J. Geophys. Res.*, 102, 16971-16988.
- Ungar, S. G. (1997). Technologies for future Landsat missions, *Photogrammetric Engineering & Remote Sensing*, 63, 901-905.
- Vane, G., Green, R. O., Chrien, T. G., Enmark, H. T., Hansen, E. G., & Porter, W. M. (1993). The Airborne Visible/Infrared Imaging Spectrometer, *Remote Sensing of the Environment*, 44, 127-143.